Supporting Information for:

Colloidal-ALD-grown core/shell CdSe/CdS Nanoplatelets as Seen by DNP Enhanced PASS-PIETA NMR Spectroscopy

Laura Piveteau,[†,‡,∥] *Dmitry N. Dirin,*[†,‡] *Christopher P. Gordon,*[†] *Brennan J. Walder,*[§] *Ta-Chung Ong,*[†,#] *Lyndon Emsley,*[§] *Christophe Copéret,*[†,*] *and Maksym V. Kovalenko.*[†,‡,*]

[†]Department of Chemistry and Applied Biosciences, ETH Zürich, Vladimir Prelog Weg 1-5, CH-8093, Switzerland.

[‡]Empa-Swiss Federal Laboratories for Materials Science and Technology, Dübendorf, Überlandstrasse 129, CH-8600, Switzerland.

[§]Institut des Sciences et Ingénierie Chimiques, Ecole Polytechnique Fédérale de Lausanne (EPFL), 1015 Lausanne, Switzerland.

*E-mail: ccoperet@ethz.ch, mvkovalenko@ethz.ch

Present addresses

[#]T.-C. Ong: Department of Chemistry and Biochemistry, University of California Los Angeles, Los Angeles, California 90095, United States.

[‖]L. Piveteau: CNRS, UPR 3079, CEMHTI, 45071 Orléans Cedex 02, France.

Table of Contents

Materials

Cadmium nitrate tetrahydrate ($Cd(NO_3)_2 \cdot 4H_2O$, Fluka, ≥99%), sodium myristate (Na(myr), TCI, ≥98%), selenium (Se, Aldrich, 100 mesh, 99.99%), cadmium acetate dihydrate ($Cd(OAc)_2 \cdot 2H_2O$, Fluka, ≥98%), oleic acid (OA, Aldrich, 90%), ammonium sulfide aqueous solution ($(NH_4)_2S$, Aldrich, 40-48%), oleylamine (OAm, Aldrich, 70%), 1-octadecene (ODE, Aldrich, 90%), N-methylformamide (MFA, TCI, >99%), formamide (FA, Aldrich, 99%), acetonitrile (ACN, Aldrich, ≥99.9%), toluene (Aldrich, ≥99.7%), hexane (Aldrich, ≥95%), ethanol (EtOH, Aldrich, ≥99.8%), methanol (MeOH, Aldrich, ≥99.9%), chloroform-d ($CDCl_3$, ≥99.8 atom% D), benzene-d^6 (C_6D_6, ≥99.5 atom% D). *Biradical polarizing agents*: TEKPol[1] and AMUPol[2] were provided by Dr. Olivier Ouari, Dr. Gilles Casano and Prof. Dr. Paul Tordo (Aix-Marseille Université). *Meso-SiO_2 matrices:* 15 nm silica (Davisil Grade 643, Aldrich), 30 nm silica gel (spherical shapes, AlfaAesar).

Methods

Synthesis Protocols

Cadmium precursor synthesis. Cadmium myristate ($Cd(myr)_2$) was synthesized by dropwise addition of 3.085 g $Cd(NO_3)_2$ (10 mmol) in 100 mL MeOH to 7.51 g Na(myr) (30 mmol) in 1 L MeOH. Precipitated $Cd(myr)_2$ was filtrated, washed twice with MeOH and dried in a vacuum oven at 50°C for 16 h.

CdSe NPL synthesis. CdSe nanoplatelets (NPLs) with emission at 511 nm were synthesized as reported elsewhere,[3-4] with slight modifications. 222 mg of $Cd(myr)_2$ (0.391 mmol), 15.7 mg of Se mesh (0.199 mmol) and 20 mL of ODE were degassed in a three-neck flask at room temperature for 30 min and heated up to 100 °C under vacuum. Then the flask was filled with argon and the mixture was quickly heated to 240 °C. When the temperature reached 190-195 °C, 52 mg of $Cd(OAc)_2$ (0.195 mmol) were introduced as a powder together with 1 mL of hexane (caution: hexane evaporates immediately!). The reaction mixture was kept at 235-240 °C for 5 min and then cooled down with air flow. When temperature dropped to 65-70 °C, 2.6 mL of OA and 3 mL of hexane were added and the mixture was stirred for additional 5 min. The obtained solution was transferred into centrifuge tubes together with 10 mL of hexane. The NPLs were separated by centrifugation at 12 krpm (19800×*g*) for 10 min. The supernatant was discarded while the precipitate, containing only NPLs, was redissolved in 1 mL hexane. This solution was additionally purified by diluting with 4 mL hexane, precipitating with 2.5 mL EtOH at 12 krpm, redispersing in 1 mL hexane and filtrating trough 0.45 μm polytetrafluoroethylene filter.

CdSe/CdS core/shell NPLs synthesis. CdSe/CdS core/shell NPLs were synthesized analogously to ref.[5] 15 mg of CdSe NPLs in 2.4 mL hexane (yellow solution) were combined with 3.6 mL of MFA and 36 μL of $(NH_4)_2S$ aqueous solution (light-yellow solution) inside a vial. The biphasic system was heavily stirred under ambient conditions for ~3-5 min. After complete phase transfer (colorless hexane phase and orange MFA phase) NPLs in MFA were rinsed three times with 2 mL of fresh hexane and precipitated with 3.6 mL ACN and 5.8 mL toluene. One third of the precipitated NPLs (corresponding to ca. 5 mg of initial CdSe NPLs) was directly redissolved in 0.1 mL MFA (**CdSe/S^{2-} in MFA sample**). The rest (10 mg of initial CdSe NPLs) was redissolved in 1 mL MFA and mixed with 1.2 mL of 0.2 M $Cd(Ac)_2$ solution in MFA. After 1 min, NPLs were precipitated with 4.4 mL toluene. Half of this precipitate (corresponding to 5 mg of initial CdSe NPLs) was redissolved in 0.1 mL MFA (**CdSe/S^{2-}/Cd^{2+}MFA sample**). The rest was redissolved in 0.28 mL hexane with 33.2 μL OAm, precipitated with 0.24 mL EtOH and redissolved in hexane (**CdSe/CdS-OAm in hexane sample**).

Computational Details

All geometry optimizations were performed with the Gaussian09 package[6] at the PBE0 level.[7] Cd and Te were represented by lanl2dz effective core potentials (ECP) and the associated basis set.[8] H, O, S, and Se atoms were represented by a by triple-ζ-tvpe basis sets.[9] NMR calculations were performed within the GIAO framework using ADF 2014[10] with the PBE0 functional and Slater-type basis sets of quadruple-ζ quality (QZ4P) on Cd and triple-ζ quality (TZ2P) on all other atoms. Relativistic effects were treated by the two-component zeroth order regular approximation (ZORA).[11-15]

Characterisation

UV/VIS/IR Absorption Spectroscopy

UV/VIS/IR absorption spectra were collected using a JASCO V670 spectrometer.

Photoluminescence Spectroscopy

A fluoromax-4 Horiba spectrofluorimeter equipped with a visible PMT detector was used to acquire the steady state photoluminescence (PL) spectra of NPL solutions. The excitation wavelength was 530 nm with a bandwidth of 1 nm.

Electrophoretic Mobility

Electrophoretic mobility was measured using a Zetasizer Nano-ZS (Malvern Instruments, Inc.). Colloidal solutions were measured using a dip-cell setup with Pd electrodes. Typical measurements of electrophoretic mobility included several scans of 100 runs each in the high-resolution mode. Dilution was optimized for each sample to achieve >100 kcps count rate and the best signal-to-noise ratio. The voltage applied to colloidal solutions was typically between 2 V and 10 V for polar solvents (MFA) and 40 V for nonpolar ones (chloroform). Table S1 summarises the zeta-potentials of the studied CdSe NPLs systems.

Table S1: Summary of the zeta-potentials of CdSe NPLs at different stages of CdS shell growth.

NPL system	CdSe-OA	CdSe/S^{2-}	CdSe/S^{2-}/Cd^{2+}	CdSe/CdS-OAm
Voltage (meV)	0	-14	+5	0

Transmission Electron Microscopy

Transmission electron microscopy (TEM) images were recorded on a JEOL JEM-2200FS microscope operated at 200 kV.

Solution-state NMR

Solution-state NMR spectra were acquired on a Bruker 11.7 T spectrometer equipped with a PABBO probe head for 5 mm NMR tubes and an Avance III console. Experiments were performed at room temperature without spinning the sample. During solution NMR experiments, the Waltz16[16-17] decoupling sequence was applied with a radio frequency (rf) field of 3 kHz. Chemical shifts were referenced to$Si(CH_3)_4$ (^1H, ^{13}C)

Detailed experimental conditions such as pulse sequence, pulse length, *etc.* are listed below in "*Details about Displayed NMR Experiments*".

DNP NMR

DNP NMR experiments were conducted on a commercial Bruker 14.1 T DNP NMR spectrometer equipped with an Avance III console and triple or double resonance 3.2 nm low temperature MAS probe. The

microwave frequency of 395 GHz was generated by a Bruker gyrotron which output an approximate microwave power of 6 W.

Cross polarization (CP) transfer[18] was conducted with variable amplitude during contact time.[19] Delay times were set to be 1.3 times the T_1 obtained from saturation recovery experiments of the protons of the solvent. The SPINAL-64 hetero-nuclear decoupling sequence[20] with a rf field of 100 kHz was used for all DNP NMR experiments. Chemical shifts were referenced to $Si(CH_3)_4$ (^1H, ^{13}C), $Cd(CH_3)_2$ ($^{111/113}Cd$).

Detailed experimental conditions such as pulse sequence, spinning frequency of the MAS, pulse length, etc. are listed below in "*Details about Displayed NMR Experiments*".

Relation of the Chemical Shift and the Electronic Structure

The dependence of the chemical shift of a semiconductor on its electronic structure, including its band gap, can be understood from theory.[21] The experimentally observed chemical shift **δ** is expressing the shielding tensor **σ** with respect to a reference compound (ref):

$$\text{chemical shift tensor component: } \delta_{\alpha\beta} = \frac{\sigma_{\alpha\beta,ref} - \sigma_{\alpha\beta}}{1 - \sigma_{\alpha\beta}} \text{ where } \alpha,\beta,\gamma = \text{Cartesian axes} \qquad (1)$$

The shielding tensor can be separated into a diamagnetic (σ_d), a paramagnetic (σ_p) and spin-orbit (σ_{SO}) component:

$$\boldsymbol{\sigma = \sigma_d + \sigma_p + \sigma_{SO}} \qquad (2)$$

The diamagnetic contribution is defined as the shielding of the observed spin from the external magnetic field by the magnetic field induced by the molecular electronic ground state structure:

$$\boldsymbol{\sigma}_d = \frac{\mu_0}{4\pi} \frac{e^2}{2m_e} \left\langle \Psi_0 \middle| \sum_i \frac{\alpha_i^2 + \beta_i^2}{r_i^3} \middle| \Psi_0 \right\rangle \qquad (3)$$

It only depends on the ground electronic state Ψ_0, summing over i electrons. r_i is the distance between the nucleus and the electron i and α_i/β_i are the distances of the electron i to the nucleus along the axes α and β. The factor r_i^3 induces a strong distance dependence of the diamagnetic shielding, whereby the nearest electrons, *i.e.* the ones of the core, have the biggest impact. The diamagnetic shielding is hence a mostly nucleus-specific shielding contribution and usually independent of the chemical environment of a spin.

The paramagnetic contribution to the shielding tensor of a spin results from the admixture of electronically excited states Ψ_j to the ground state Ψ_0 by action of the magnetic angular momentum operator $\hat{l}_n$ of a spin *n*. It can be well described in a 2nd order perturbation approach:[22]

$$\sigma_{nm}^p = -\frac{\mu_0}{4\pi} \frac{e^2}{2m_e} \sum_{j \neq 0} \left[\frac{\left\langle \Psi_0 \middle| \sum_i \hat{l}_{in} \middle| \Psi_j \right\rangle \left\langle \Psi_j \middle| \sum_i \frac{\hat{l}_{im}}{r_i^3} \middle| \Psi_0 \right\rangle + \left\langle \Psi_j \middle| \sum_i \frac{\hat{l}_{im}}{r_i^3} \middle| \Psi_0 \right\rangle^* \left\langle \Psi_0 \middle| \sum_i \hat{l}_{in} \middle| \Psi_j \right\rangle^*}{E_j - E_0} \right] \qquad (4)$$

In semiconductor materials, Ψ_0 represents the wave function of electrons in the valence band at the energy E_0 and Ψ_j represents the wave function of electrons in the conduction band at the energy E_j. Consequently, $E_j - E_0$ is equivalent to the band gap energy, which eventually is inversely proportional to the chemical shift.

For heavy atoms, spin-orbit coupling significantly influences their shielding tensor and it has therefore to be included in the theoretical treatment of the chemical shielding. Spin-orbit coupling arises from the magnetic interaction of the electron spin angular momentum with the electron orbital angular momentum and is particularly strong in systems with heavy nuclei, where the velocity of electrons in the core region is high. The spin-orbit interaction can be treated by perturbation theory to third order, by a coupling of the singlet ground state with triplet excited states in combination with Fermi-contact and spin-dipole hyperfine ineteractions. This interaction leads to a deformation of the electron density as well as to a magnetically induced spin density, which influence the NMR chemical shift.[23-24]

The totality of the DFT calculations performed for this work are listed in Table S2, S3 and S4.

Table S2. Comparison of the calculated total shielding and shielding contributions of the octahedral hexa-aqua cadmium complex $[Cd(OH_2)_6]^{2+}$ and the tetrahedral tetra-aqua cadmium complex $[Cd(OH_2)_4]^{2+}$. All shielding values are indicated in ppm.

	$[Cd(OH_2)_6]^{2+}$	**$[Cd(OH_2)_4]^{2+}$**
total shielding σ_{iso}	4314	4368
diamagnetic contribution σ_{dia}	4817	4819
paramagnetic contribution σ_{para}	-1046	-992
spin-orbit contribution σ_{SO}	543	541

Table S3. Summary of the calculated total shielding and shielding contributions of all tetrahedral compounds with formula $[Cd(XH_2)_n(YH_2)_{4-n}]^{2+}$ (X, Y = O, S, Se, Te) with n = 0 - 4. All shielding values are indicated in ppm.

Shielding contribution	**σ_{iso}**	**σ_{dia}**	**σ_{para}**	**σ_{SO}**
$[Cd(OH_2)_4]^{2+}$	4368	4819	-992	541
$[Cd(OH_2)_3(SH_2)]^{2+}$	4255	4822	-1110	543
$[Cd(OH_2)_2(SH_2)_2]^{2+}$	4135	4825	-1239	549
$[Cd(OH_2)(SH_2)_3]^{2+}$	4026	4828	-1358	556
$[Cd(OH_2)_3(SeH_2)]^{2+}$	4278	4821	-1115	572
$[Cd(OH_2)_2(SeH_2)_2]^{2+}$	4160	4824	-1267	603
$[Cd(OH_2)(SeH_2)_3]^{2+}$	4058	4827	-1407	638
$[Cd(SH_2)_4]^{2+}$	3915	4831	-1477	561
$[Cd(SH_2)_3(SeH_2)]^{2+}$	3931	4830	-1487	588
$[Cd(SH_2)_2(SeH_2)_2]^{2+}$	3949	4830	-1498	617
$[Cd(SH_2)(SeH_2)_3]^{2+}$	3956	4829	-1515	642
$[Cd(SeH_2)_4]^{2+}$	3965	4829	-1531	667
$[Cd(OH_2)_3(TeH_2)]^{2+}$	4320	4822	-1123	622
$[Cd(OH_2)_2(TeH_2)_2]^{2+}$	4202	4824	-1316	694
$[Cd(OH_2)(TeH_2)_3]^{2+}$	4123	4826	-1478	775
$[Cd(TeH_2)_4]^{2+}$	4079	4829	-1596	846
$[Cd(SH_2)_3(TeH_2)]^{2+}$	3962	4830	-1506	637
$[Cd(SH_2)_2(TeH_2)_2]^{2+}$	4000	4830	-1536	706
$[Cd(SH_2)(TeH_2)_3]^{2+}$	4045	4829	-1567	784
$[Cd(SeH_2)_3(TeH_2)]^{2+}$	3990	4829	-1550	711

$[Cd(SeH_2)_2(TeH_2)_2]^{2+}$	4023	4829	-1567	761
$[Cd(SeH_2)(TeH_2)_3]^{2+}$	4050	4829	-1583	804

Table S4. Summary of the calculated chemical shielding tensor components and therefrom derived chemical shielding anisotropy (CSA) parameters for all compounds with formula $[Cd(XH_2)_n(YH_2)_{4-n}]^{2+}$ (X, Y = O, S, Se, Te) with n = 0 - 4. All shielding values are indicated in ppm.

	σ_{11}	σ_{22}	σ_{33}	σ_{iso}	Δ	η
$[Cd(OH_2)_4]^{2+}$	4358	4358	4386	4368	19	0.00
$[Cd(OH_2)_3(SH_2)]^{2+}$	4121	4136	4509	4255	254	0.06
$[Cd(OH_2)_2(SH_2)_2]^{2+}$	3939	4087	4380	4135	245	0.60
$[Cd(OH_2)(SH_2)_3]^{2+}$	3813	4106	4159	4026	-213	0.25
$[Cd(OH_2)_3(SeH_2)]^{2+}$	4123	4151	4559	4278	281	0.10
$[Cd(OH_2)_2(SeH_2)_2]^{2+}$	3933	4128	4420	4160	260	0.75
$[Cd(OH_2)(SeH_2)_3]^{2+}$	3874	4140	4158	4058	-183	0.10
$[Cd(SH_2)_4]^{2+}$	3917	3917	3910	3915	-5	0.00
$[Cd(SH_2)_3(SeH_2)]^{2+}$	3927	3932	3935	3931	-4	0.69
$[Cd(SH_2)_2(SeH_2)_2]^{2+}$	3887	3959	3999	3949	-61	0.65
$[Cd(SH_2)(SeH_2)_3]^{2+}$	3918	3962	3988	3956	-38	0.68
$[Cd(SeH_2)_4]^{2+}$	3955	3955	3984	3965	19	0.00
$[Cd(OH_2)_3(TeH_2)]^{2+}$	4114	4301	4544	4320	224	0.83
$[Cd(OH_2)_2(TeH_2)_2]^{2+}$	3934	4252	4420	4202	-268	0.63
$[Cd(OH_2)(TeH_2)_3]^{2+}$	3957	4187	4226	4123	-166	0.23
$[Cd(TeH_2)_4]^{2+}$	4043	4043	4151	4079	72	0.00
$[Cd(SH_2)_3(TeH_2)]^{2+}$	3910	3939	4036	3962	74	0.39
$[Cd(SH_2)_2(TeH_2)_2]^{2+}$	3889	4018	4095	4000	-112	0.69
$[Cd(SH_2)(TeH_2)_3]^{2+}$	3974	4030	4132	4045	87	0.65
$[Cd(SeH_2)_3(TeH_2)]^{2+}$	3945	3969	4057	3990	67	0.36
$[Cd(SeH_2)_2(TeH_2)_2]^{2+}$	3956	4007	4107	4023	84	0.61
$[Cd(SeH_2)(TeH_2)_3]^{2+}$	3986	4031	4132	4050	82	0.55

Supplementary Figures

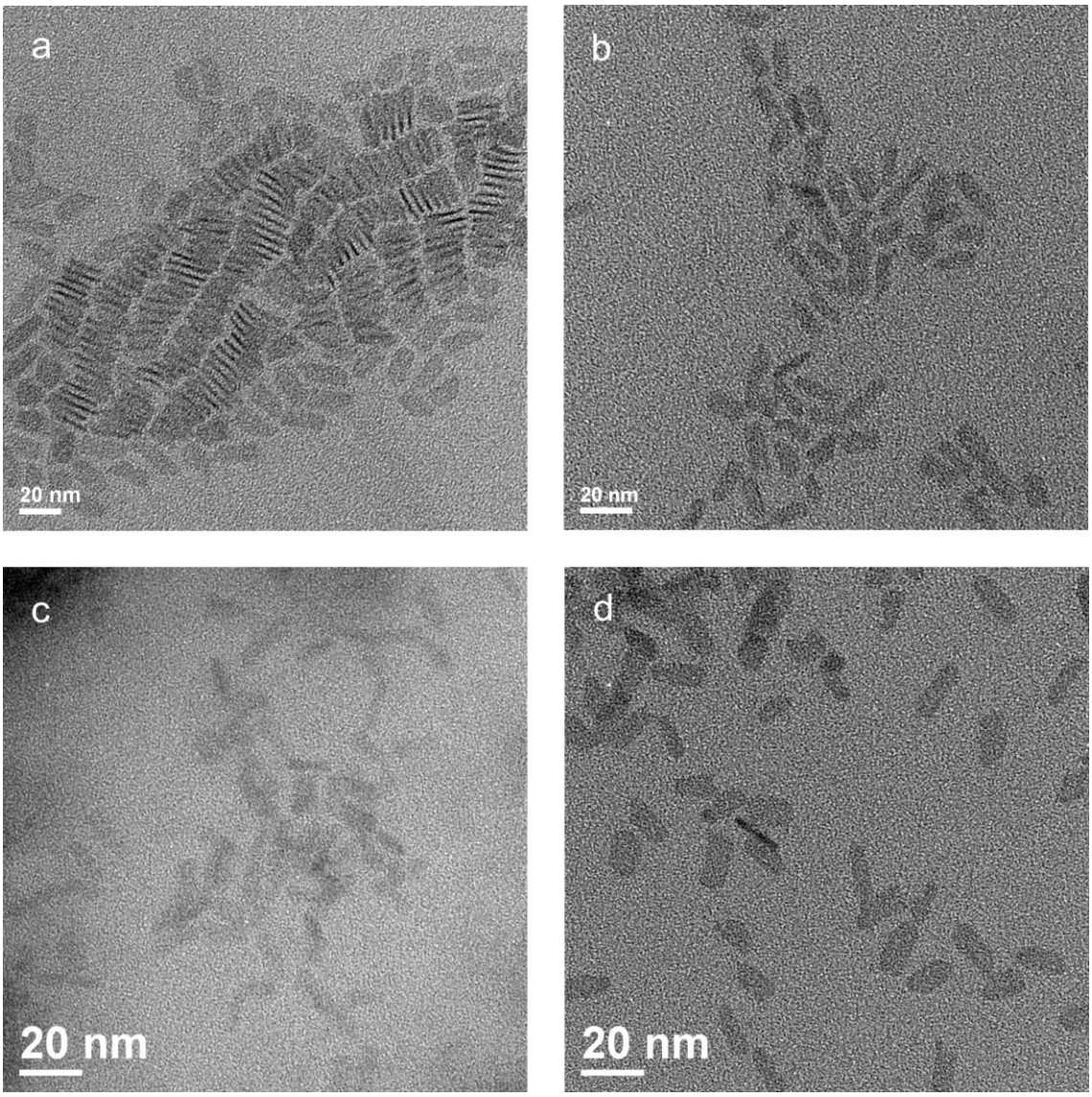

Figure S1: TEM images of zinc-blende (ZB) CdSe NPLs at the investigated stages of c-ALD: CdSe-OA NPLs in hexane (a), CdSe/S^{2-} in MFA (b), CdSe/S^{2-}/Cd^{2+} NPLs in MFA (c) and CdSe/CdS-OAm NPLs in hexane (d).

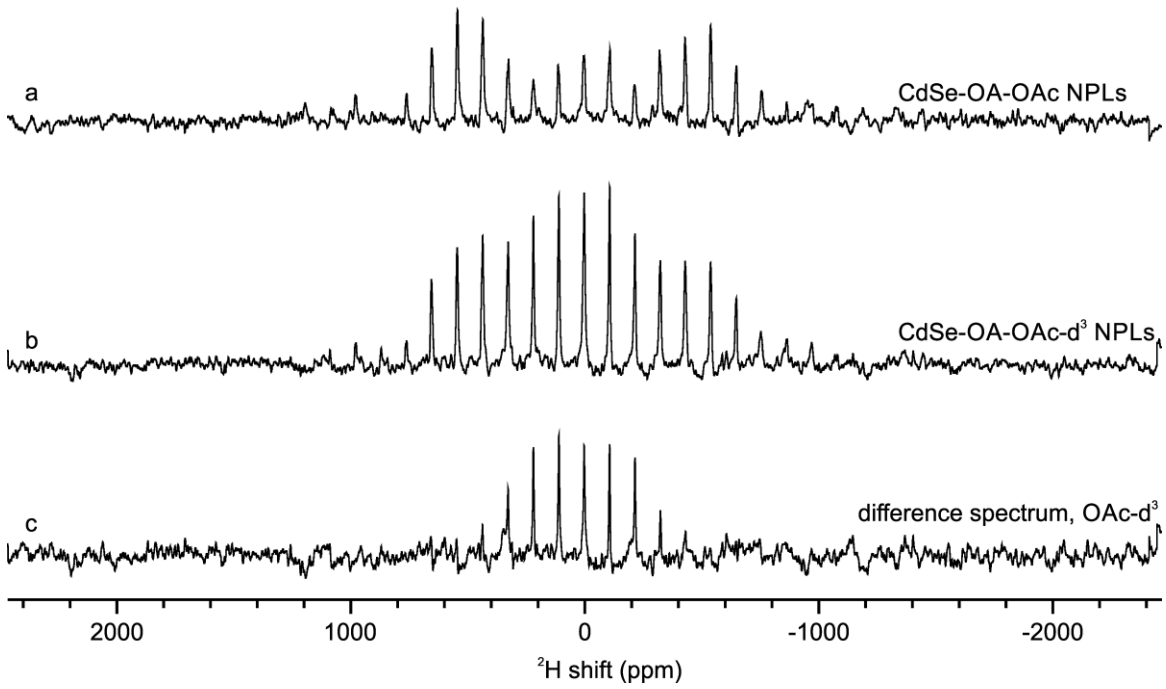

Figure S2. ^{2}H CP DNP NMR spectra evidencing the presence of acetate ligands at the CdSe NPL surface. (a) The ^{2}H DNP NMR spectrum of conventional ZB CdSe NPLs capped with carboxylate ligands acquired at a spinning speed of 10 kHz. Naturally abundant ^{2}H of the oleate/myristate is assumed to be responsible for the signal in (a) since ^{2}H signal from the solvent (TCE) was reported to be very weak.[25] If deuterated cadmium acetate ($Cd(OAc\text{-}d^3)_2$) is used during the ZB CdSe NPL synthesis, no split signal is observed. Instead, a broad signal of a similar width is found (b). The difference between the two spectra (c) must correspond to the signal from deuterated acetate as the two synthetic procedures were identical except for the degree of deuteration of the cadmium acetate. The absence of free ligands was verified with liquid NMR, where no signal from free ligands was found (not shown). Neither was there a signal of free cadmium carboxylate around -680 ppm in the ^{113}Cd DNP NMR spectrum (reference spectra of free $Cd(OAc)_2$ in formamide (FA), MFA, DNP juice [60:30:10 (v/v) of glycerol-d^8/D_2O/H_2O], OAm and $Cd(oleate)_2$ in TCE-ODE mixture are shown in Figure S5). Furthermore, acetate is insoluble in the apolar solvent in which the NPLs were solubilized, *i.e.* 1,1,2,2-tetrachloroethane (TCE). Therefore, we can conclude that the additional deuterium signal must originate from deuterated acetate OAc-d^3 binding to the NPL's surface.

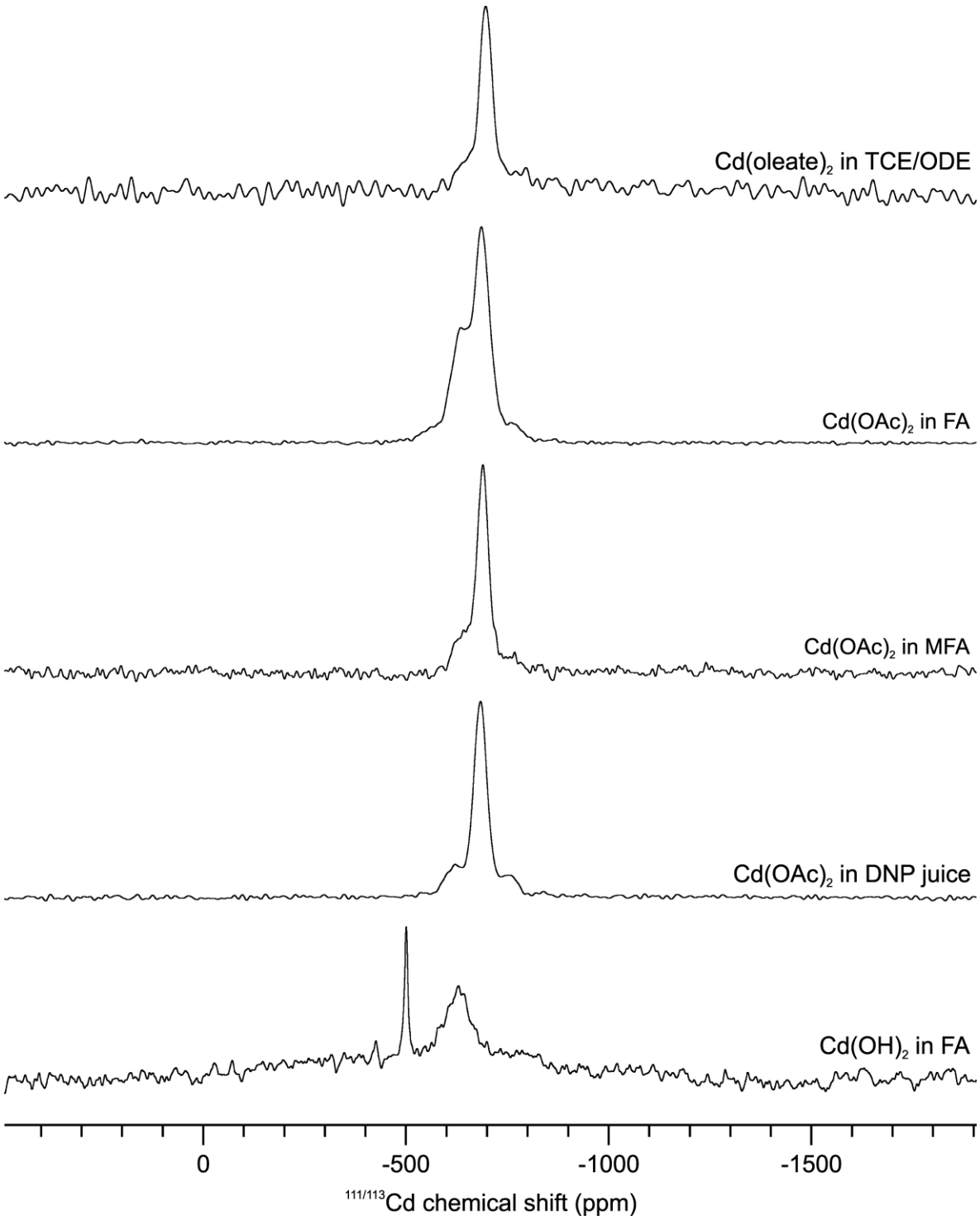

Figure S3: $^{111/113}$Cd DNP NMR spectra of $Cd(OAc)_2$ in FA (-688 ppm, shoulder at -637 ppm), $Cd(OAc)_2$ DNP juice (-685 ppm), $Cd(OH)_2$ in FA (broad signal at -623 ppm from dissolved cadmium, sharp peak at -495 ppm from crystalline, non-dissolved $Cd(OH)_2$) and $Cd(oleate)_2$ in TCE/ODE (-694 ppm). ^{113}Cd low-temperature spectrum of $Cd(OAc)_2$ in MFA (-693 ppm). DNP juice consists of 60:30:10 (v/v) of glycerol-d^8/D_2O/H_2O.

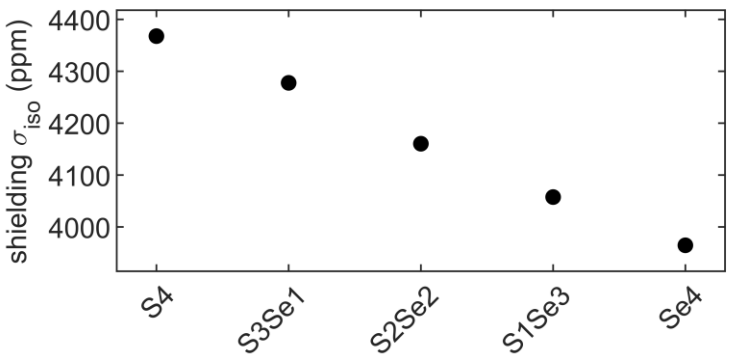

Figure S4: Graph displaying the linear trend when gradually exchanging SH_2 ligands with SeH_2 ligands in cadmium complexes with formula $[Cd(SH_2)_{4-n}(SeH_2)_n]^{2+}$ where n = 0-4. The ligands coordinating to the cadmium atoms are indicated in the x-axis whereby S = SH_2 and Se = SeH_2. The raw data can be found in Table S3.

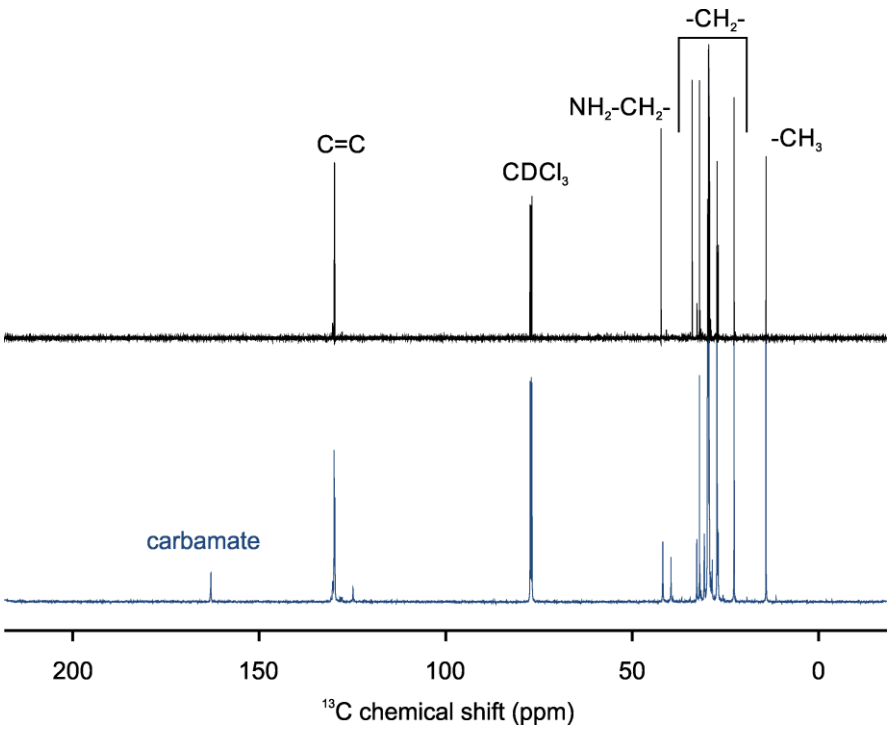

Figure S5: Formation of carbamate (blue, bottom) from OAm in $CDCl_3$ (black, top) was achieved by adding dry ice to the solution. The characteristic carbonyl peak is observed at 163 ppm (H**C**OO-NH_2-CH_2-). However, conversion is incomplete as in the heteroatom bound region of the spectrum not only carbamate signal is found (39 ppm, HCOO-NH_2-**C**H_2-) but also OAm signal (42 ppm, NH_2-**C**H_2-).

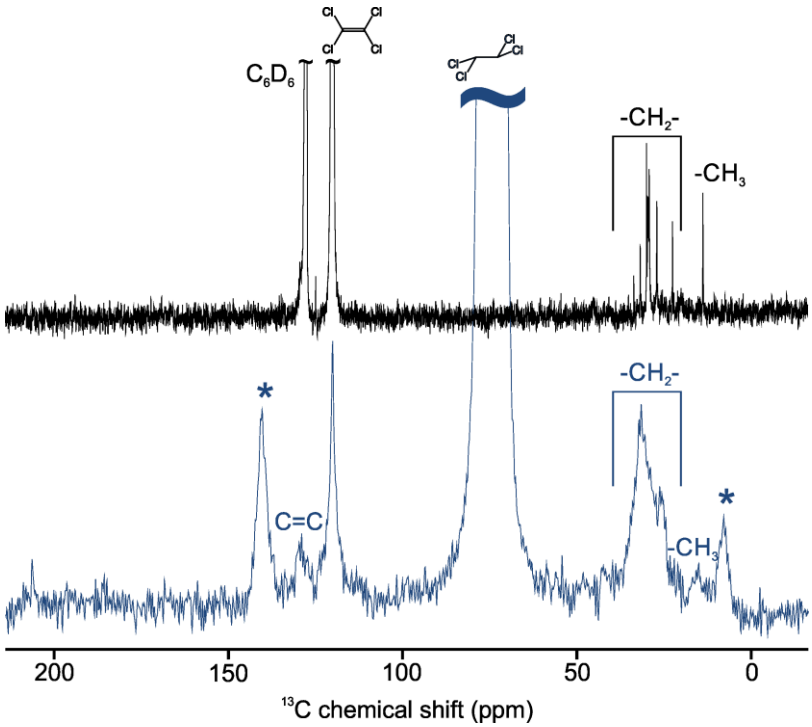

Figure S6: ^{13}C solution (top, black) and DNP (bottom, blue) NMR spectra of core/shell CdSe/CdS-OAm NPLs. Due to slow tumbling of the NPLs, only the end of the aliphatic chain is visible in the solution spectrum, proving that the olyelamine is surface bound. The DNP spectrum displays the C=C double bond signal at 130 ppm. The absence of a carbonyl signal (180-185 ppm) and the absence of a carbamate signal (160-165 ppm) is indicating that no oleic acid nor carbamate is bound to the surface. However, the absence of carbonyl signal is not contradictory to the presence of acetate at the surface as the rotation of the methyl group might lead to the loss of carbonyl acetate signal by accelerated relaxation.[26-27]

Details about Sideband Pattern Fit to Extract CSA Parameters

The chemical shift anisotropy (CSA) parameters of the species from the spectra presented in Figure 3 and listed in Table 1, were obtained by fitting the sideband patterns in the indirect dimension of the 2D PASS spectrum in their respective isotropic chemical shift region. The approximate probability distributions for each of the line shape parameters were determined using ordinary least square maximum likelihood estimation, utilizing a χ^2 scaled Markov chain Monte Carlo method to sample the parameter space. Three different models were used to simulate the sideband order spectra. For sites without significant anisotropy, an upper bound on the strength of the anisotropy $|\Delta|$ was determined by modeling the line shape with a single CSA tensor subject to the constraint $\eta = 1$. The lower bound is assumed to be zero since this model is susceptible to overfitting noise riding the $k = \pm 1$ order sideband intensities. For the remaining sites, the sideband intensity profiles were modeled according to the Δ and η parameters of a single CSA tensor. In two cases ($CdSe/S^{2-}$ and the broad feature of CdSe/CdS-OLA), the sideband profile of the integrated isotropic region also contains a contribution from species without significant anisotropy; here, the CSA parameters of the significant contribution were estimated by assuming that $\Delta = 0$ for the site with small CSA. This was achieved by masking the centerband from the fit to the sideband profile. All ranges reported correspond to approximate 95% confidence regions. A '(±)' symbol indicates that the sign of δ is ambiguous, which occurs when η is predicted to be unity.

The fit results are summarized for all four stages of c-ALD (CdSe-OA, $CdSe/S^{2-}$, CdSe/S/Cd and CdSe/CdS-OAm) in the figures below (Figure S7, Figure S8, Figure S9 and Figure S10).

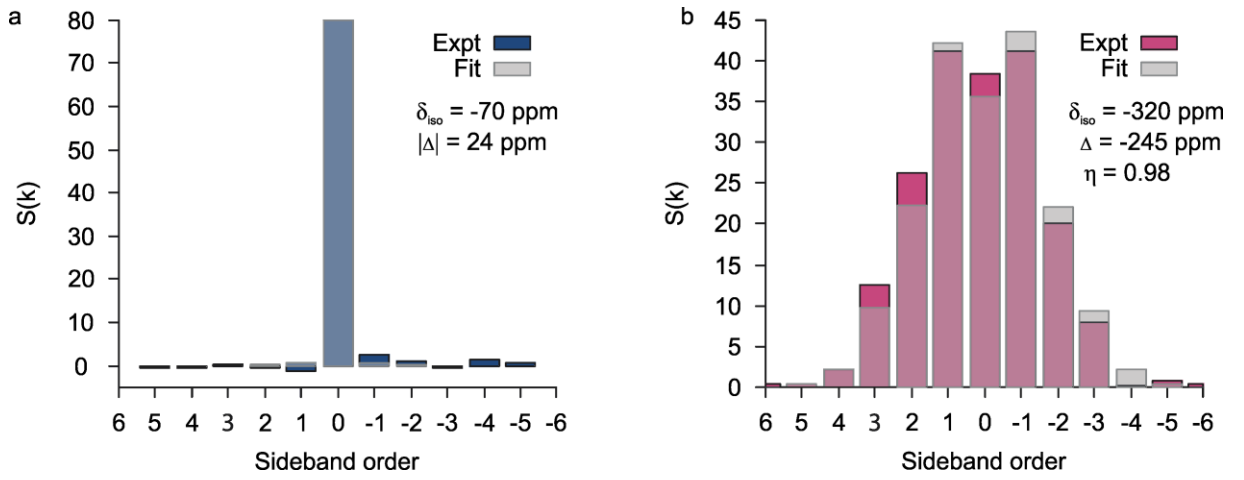

Figure S7. Sideband patterns and fits thereof of the core (a) and surface (b) species of oleate-capped ZB CdSe NPLs. The CSA parameter values obtained from the fit are listed below the legends. The color code is the same as in Figure 3.

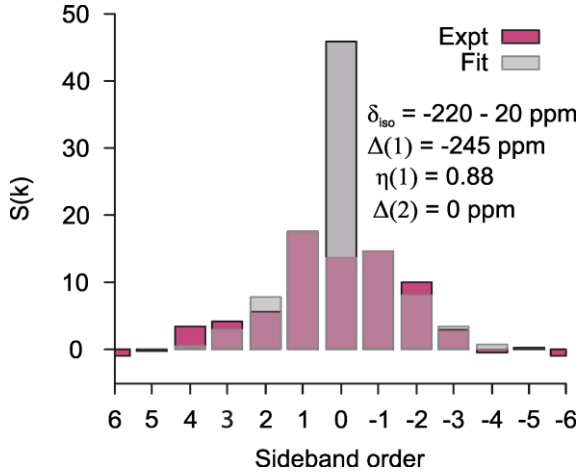

Figure S8. Sideband pattern and fit thereof of the core species of sulfide-capped CdSe NPLs in MFA. The CSA parameter values obtained from the fit are listed below the legend. The color code is the same as in Figure 3.

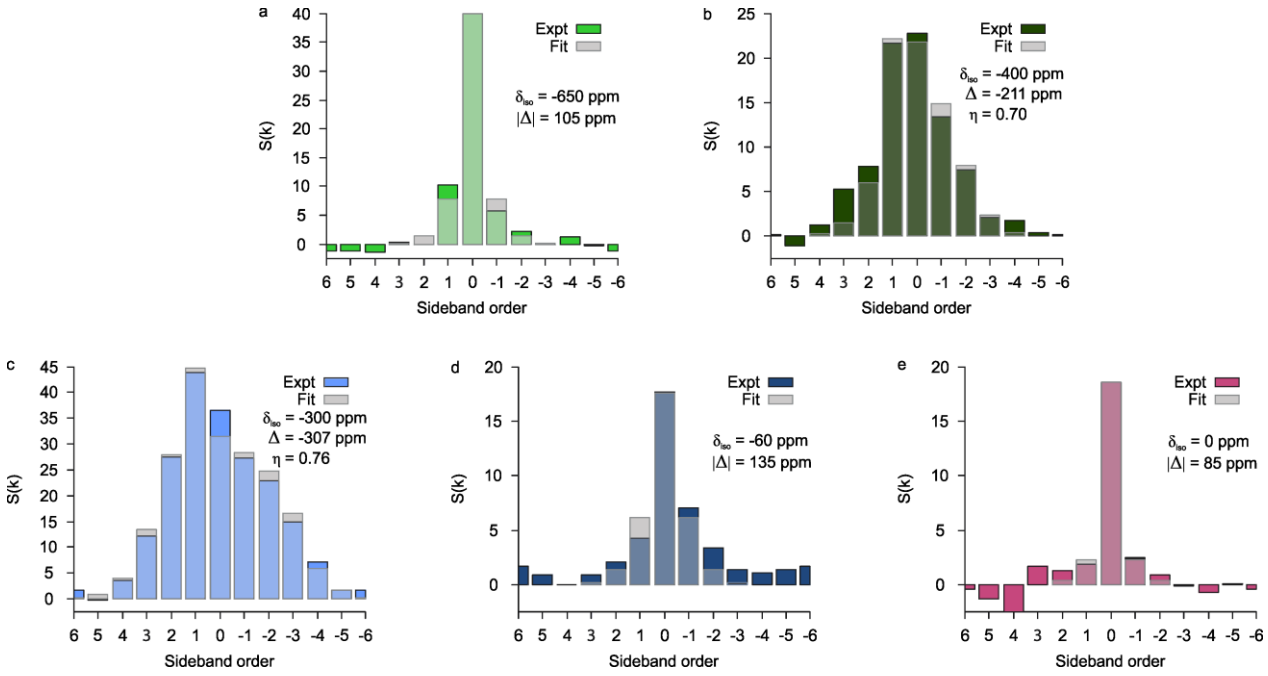

Figure S9. Sideband patterns and fits thereof of free $Cd(OAc)_2$ (a), naked surface Cd (b), surface Cd-acetate (c), core CdSe (d) and core CdS (e) in $CdSe/S^{2-}/Cd^{2+}$ colloidal NPL solutions in MFA. The CSA parameter values obtained from the fits are listed below the legends. The color code is the same as in Figure 3.

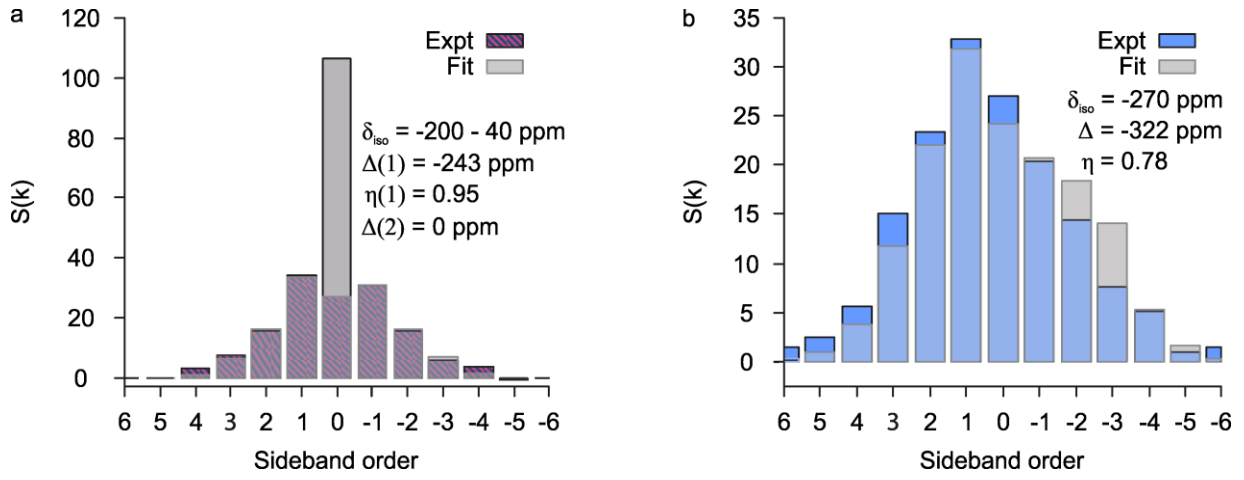

Figure S10. Sideband patterns and fits thereof of the core (a) and surface (b) species of oleylamine-capped CdSe/CdS core/shell NPLs. The CSA parameter values obtained from the fit are listed below the legends. The color code is the same as in Figure 3.

Details about Displayed NMR Experiments

Figure 1 and 3: CdSe-OA NPLs in hexane

Approximatively 3 mg of ZB CdSe-OA NPLs in 1,1,2,2-tetrachloroethane (TCE, 12.7 µL) were mixed with 6.3 µL 50 mM TEKPol in TCE on a watch glass yielding a final TEKPol concentration of 16 mM. Minimal amount of meso-SiO_2 (30 nm pore size) was impregnated with the radical-QD solution and then packed into a 3.2 mm sapphire rotor.

Acquisition parameters for ^{113}Cd DNP enhanced PASS-PIETA	
Magnetic field	14.1 T
Temperature	100 K
Rotor diameter (mm)	3.2
Pulse Sequence	CP-PASS-PIETA
Number of scans	18
Recycle delay (s)	6.8
Spectral width (kHz)	625
Spinning frequency (Hz)	10000
Acquisition length (number of points)	1220
^{1}H 90° pulse width [π/2] (µs)	2.5
Contact pulse length (ms)	14.0
^{1}H rf field during contact pulse (kHz)	100
^{113}Cd rf field during contact pulse (kHz)	63
^{113}Cd 90° pulse width [π/2] (µs)	3.2
Number of pass steps	12
Number of echos	40
Number of phases	48

Figure 3: CdSe/S^{2-} in MFA

Approximatively 2.5 mg of CdSe/S^{2-} NPLs in MFA (50 µL) were impregnated with meso-SiO_2 (30 nm pore size) and washed twice with 1.5 mL fresh toluene in order to remove all MFA. The meso-SiO_2 was dried under vacuum until complete evaporation of the toluene. Finally, minimal amount of the CdSe-silica was impregnated with 20 µL 16 mM TEKPol solution in TCE and packed into a 3.2 mm sapphire rotor.

Acquisition parameters for ^{113}Cd DNP enhanced PASS-PIETA	
Magnetic field	14.1 T
Temperature	100 K
Rotor diameter (mm)	3.2
Pulse Sequence	CP-PASS-PIETA
Number of scans	80
Recycle delay (s)	5.3
Spectral width (kHz)	625
Spinning frequency (Hz)	10000
Acquisition length (number of points)	1220
^{1}H 90° pulse width [π/2] (µs)	2.5
Contact pulse length (ms)	14.0
^{1}H rf field during contact pulse (kHz)	100
^{113}Cd rf field during contact pulse (kHz)	63
^{113}Cd 90° pulse width [π/2] (µs)	3.2

Number of pass steps	12
Number of echos	40
Number of phases	48

Figure 3: Core/Shell CdSe/S/Cd in MFA

Approximatively 2.5 mg of core/shell CdSe/S^{2-}/Cd^{2+} in MFA (50 µL) were impregnated with meso-SiO_2 (30 nm pore size) and washed twice with 1.5 mL fresh toluene in order to remove all MFA. The meso-SiO_2 was dried under vacuum until complete evaporation of the toluene. Finally, minimal amount of the CdSe-silica was impregnated with 20 µL 16 mM TEKPol solution in TCE and packed into a 3.2 mm sapphire rotor.

Acquisition parameters for ^{113}Cd DNP enhanced PASS-PIETA	
Magnetic field	14.1 T
Temperature	100 K
Rotor diameter (mm)	3.2
Pulse Sequence	CP-PASS-PIETA
Number of scans	24
Recycle delay (s)	6.2
Spectral width (kHz)	625
Spinning frequency (Hz)	10000
Acquisition length (number of points)	1220
^{1}H 90° pulse width [π/2] (µs)	2.5
Contact pulse length (ms)	14.0
^{1}H rf field during contact pulse (kHz)	100
^{113}Cd rf field during contact pulse (kHz)	63
^{113}Cd 90° pulse width [π/2] (µs)	2.8
Number of pass steps	12
Number of echos	40
Number of phases	48

Figure 3: Core/shell CdSe/CdS-OAm NPLs in hexane

Approximatively 2 mg of core/shell CdSe/CdS-OAm NPLs in TCE (12.7 µL) were mixed with 6.3 µL 50 mM TEKPol in TCE on a watch glass yielding a final radical concentration of 16 mM. Minimal amount of meso-SiO_2 (30 nm pore size) was impregnated with the radical-NPL solution and then packed into a 3.2 mm sapphire rotor.

Acquisition parameters for ^{113}Cd DNP enhanced PASS-PIETA	
Magnetic field	14.1 T
Temperature	100 K
Rotor diameter (mm)	3.2
Pulse Sequence	CP-PASS-PIETA
Number of scans	24
Recycle delay (s)	5.5
Spectral width (kHz)	625
Spinning frequency (Hz)	10000
Acquisition length (number of points)	1220
^{1}H 90° pulse width [π/2] (µs)	2.5
Contact pulse length (ms)	14.0
^{1}H rf field during contact pulse (kHz)	100
^{113}Cd rf field during contact pulse (kHz)	63

^{113}Cd 90° pulse width [π/2] (μs)	3.2
Number of pass steps	12
Number of echos	40
Number of phases	48

Figure S2: ZB CdSe NPLs

Approximatively 1.5 mg of ZB CdSe-OA NPLs in TCE (12.7 µL) were mixed with 6.3 µL 50 mM TEKPol in TCE on a watch glass yielding a final TEKPol concentration of 16 mM. Minimal amount of meso-SiO_2 (30 nm pore size) was impregnated with the radical-QD solution and then packed into a 3.2 mm sapphire rotor.

Acquisition parameters for ^{2}H DNP NMR	
Magnetic field	14.1 T
Temperature	100 K
Rotor diameter (mm)	3.2
Pulse Sequence	CP
Number of scans	1024
Recycle delay (s)	10.3
Spectral width (kHz)	455
Spinning frequency (Hz)	10000
Acquisition length (number of points)	36318
^{1}H 90° pulse width [π/2] (μs)	2.5
Contact pulse length (ms)	4.0
^{1}H rf field during contact pulse (kHz)	100
^{2}H rf field during contact pulse (kHz)	42

Figure S3: $Cd(OA)_2$ in TCE/ODE

12.7 µL of $Cd(OA)_2$ in ODE prepared from CdO and oleic acid was mixed with 6.3 µL 50 mM TEKPol in TCE and directly transferred into a 3.2 mm sapphire rotor. No meso-SiO_2 was added.

Acquisition parameters for ^{111}Cd DNP NMR	
Magnetic field	14.1 T
Temperature	100 K
Rotor diameter (mm)	3.2
Pulse Sequence	CP-echo
Number of scans	1024
Recycle delay (s)	5.1
Spectral width (kHz)	385
Spinning frequency (Hz)	10000
Acquisition length (number of points)	9326
^{1}H 90° pulse width [π/2] (μs)	2.5
Contact pulse length (ms)	10.0
^{1}H rf field during contact pulse (kHz)	94
^{111}Cd rf field during contact pulse (kHz)	44

Figure S3: $Cd(OAc)_2$ in FA

A saturated solution of $Cd(OAc)_2$ in FA was diluted to half. 12.7 µL of the diluted solution was complemented with 6.3 µL 50 mM AMUPol in FA. Minimal amount of meso-SiO_2 (15 nm pore size) was impregnated with the radical-QD solution and then packed into a 3.2 mm sapphire rotor.

Acquisition parameters for ^{111}Cd DNP NMR	
Magnetic field	14.1 T
Temperature	100 K
Rotor diameter (mm)	3.2
Pulse Sequence	CP-echo
Number of scans	20480
Recycle delay (s)	4.5
Spectral width (kHz)	385
Spinning frequency (Hz)	10000
Acquisition length (number of points)	9326
^{1}H 90° pulse width [π/2] (μs)	2.8
Contact pulse length (ms)	8.0
^{1}H rf field during contact pulse (kHz)	84
^{111}Cd rf field during contact pulse (kHz)	31

Figure S3: $Cd(OAc)_2$ in MFA

Approximatively 2.5 mg $Cd(OAc)_2$ were dispersed in 20 µL MFA. After impregnation with minimal amount of meso-SiO_2 (15 nm pore size) the sample was packed into a 3.2 mm sapphire rotor.

Acquisition parameters for ^{113}Cd NMR	
Magnetic field	14.1 T
Temperature	100 K
Rotor diameter (mm)	3.2
Pulse Sequence	CP-echo
Number of scans	1024
Recycle delay (s)	5.0
Spectral width (kHz)	333
Spinning frequency (Hz)	10000
Acquisition length (number of points)	8096
^{1}H 90° pulse width [π/2] (μs)	2.5
Contact pulse length (ms)	14.0
^{1}H rf field during contact pulse (kHz)	94
^{113}Cd rf field during contact pulse (kHz)	30

Figure S3: $Cd(OAc)_2$ in DNP juice

A saturated solution of $Cd(OAc)_2$ in DNP juice (60:30:10 (v/v) of glycerol-d^8/D_2O/H_2O, 10 mM AMUPol) was directly charged into a 3.2 mm sapphire rotor. No meso-SiO_2 was added.

Acquisition parameters for ^{111}Cd DNP NMR	
Magnetic field	14.1 T
Temperature	100 K
Rotor diameter (mm)	3.2
Pulse Sequence	CP-echo
Number of scans	16
Recycle delay (s)	4.5
Spectral width (kHz)	385
Spinning frequency (Hz)	10000
Acquisition length (number of points)	9326
^{1}H 90° pulse width [π/2] (μs)	2.8
Contact pulse length (ms)	8.5

^{1}H rf field during contact pulse (kHz)	84
^{111}Cd rf field during contact pulse (kHz)	29

Figure S3: $Cd(OH)_2$ in FA

A highly concentrated $Cd(OH)_2$ solution in FA (12.7 µL) was mixed with 6.3 µL 50 mM AMUPol in FA on a watch glass yielding a final AMUPol concentration of 16 mM. Minimal amount of meso-SiO_2 (30 nm pore size) was impregnated with the radical-sample solution and then packed into a 3.2 mm sapphire rotor

Acquisition parameters for ^{113}Cd DNP NMR	
Magnetic field	14.1 T
Temperature	100 K
Rotor diameter (mm)	3.2
Pulse Sequence	CP-echo
Number of scans	2048
Recycle delay (s)	12.0
Spectral width (kHz)	167
Spinning frequency (Hz)	10000
Acquisition length (number of points)	8192
^{1}H 90° pulse width [π/2] (µs)	2.5
Contact pulse length (ms)	8.0
^{1}H rf field during contact pulse (kHz)	100
^{113}Cd rf field during contact pulse (kHz)	32

Figure S5: Oleylamine solution in $CDCl_3$

One drop of as-purchased oleylamine was diluted in 400 µL $CDCl_3$.

Acquisition parameters for ^{13}C-{^{1}H}-solution NMR	
Magnetic field	11.7 T
Temperature	298 K
Tube diameter (mm)	5
Pulse Sequence	zgpg30
Number of scans	256
Recycle delay (s)	2.0
Spectral width (kHz)	30
Spinning frequency (Hz)	0
Acquisition length (number of points)	297616
^{13}C 90° pulse width [π/2] (µs)	9.5

Figure S5: oleylamine saturated with CO_2

One drop of as-purchased oleylamine was diluted in 400 µL $CDCl_3$ and several grams of dry ice were added to the solution. Before starting the NMR measurement complete sublimation of the CO_2 was awaited.

Acquisition parameters for ^{13}C solution NMR	
Magnetic field	11.7 T
Temperature	298 K
Tube diameter (mm)	5
Pulse Sequence	zgpg30

Number of scans	512
Recycle delay (s)	2.0
Spectral width (kHz)	30
Spinning frequency (Hz)	0
Acquisition length (number of points)	297616
^{13}C 90° pulse width [π/2] (μs)	9.5

Figure S6: Core/shell CdSe/CdS-OAm NPLs in hexane

Oleylamine-capped core/shell CdSe/CdS NPLs were dissolved in tetrachloroethylene and a sealed capillary containing C_6D_6 was added into the NMR tube for locking the NMR signal.

Acquisition parameters for ^{13}C-{^{1}H} solution NMR	
Magnetic field	11.7 T
Temperature	298 K
Tube diameter (mm)	5
Pulse Sequence	zgpg30
Number of scans	8192
Recycle delay (s)	2.0
Spectral width (kHz)	30
Spinning frequency (Hz)	0
Acquisition length (number of points)	297616
^{13}C 90° pulse width [π/2] (μs)	9.5

Figure S6: Core/shell CdSe/CdS-OAm NPLs in hexane

Core/shell CdSe/CdS-OAm NPLs in TCE (12.7 μL) were mixed with 6.3 μL 50 mM TEKPol in TCE on a watch glass yielding a final TEKPol concentration of 16 mM. Minimal amount of meso-SiO_2 (30 nm pore size) was impregnated with the radical-NPL solution and then packed into a 3.2 mm sapphire rotor.

Acquisition parameters for ^{13}C DNP NMR	
Magnetic field	14.1 T
Temperature	100 K
Rotor diameter (mm)	3.2
Pulse Sequence	CP-echo
Number of scans	1024
Recycle delay (s)	10.0
Spectral width (kHz)	385
Spinning frequency (Hz)	10000
Acquisition length (number of points)	9326
^{1}H 90° pulse width [π/2] (μs)	2.8
Contact pulse length (ms)	7.0
^{1}H rf field during contact pulse (kHz)	84
^{113}Cd rf field during contact pulse (kHz)	15
^{113}Cd 180° pulse width [π] (μs)	11.8

References

1. Zagdoun, A.; Casano, G.; Ouari, O.; Schwarzwälder, M.; Rossini, A. J.; Aussenac, F.; Yulikov, M.; Jeschke, G.; Copéret, C.; Lesage, A.; Tordo, P.; Emsley, L., Large Molecular Weight Nitroxide Biradicals Providing Efficient Dynamic Nuclear Polarization at Temperatures up to 200 K. *J. Am. Chem. Soc.* **2013,** *135* (34), 12790-12797.
2. Sauvée, C.; Rosay, M.; Casano, G.; Aussenac, F.; Weber, R. T.; Ouari, O.; Tordo, P., Highly Efficient, Water-Soluble Polarizing Agents for Dynamic Nuclear Polarization at High Frequency. *Angew. Chem.* **2013,** *125* (41), 11058-11061.
3. Ithurria, S.; Tessier, M. D.; Mahler, B.; Lobo, R. P. S. M.; Dubertret, B.; Efros, A. L., Colloidal Nanoplatelets with Two-Dimensional Electronic Structure. *Nat. Mater.* **2011,** *10*, 936-941.
4. Ithurria, S.; Talapin, D. V., Colloidal Atomic Layer Deposition (c-ALD) using Self-Limiting Reactions at Nanocrystal Surface Coupled to Phase Transfer between Polar and Nonpolar Media. *J. Am. Chem. Soc.* **2012,** *134* (45), 18585-18590.
5. She, C.; Fedin, I.; Dolzhnikov, D. S.; Demortière, A.; Schaller, R. D.; Pelton, M.; Talapin, D. V., Low-Threshold Stimulated Emission Using Colloidal Quantum Wells. *Nano Lett.* **2014,** *14* (5), 2772-2777.
6. Frisch, M. J.; Trucks, G. W.; Schlegel, H. B.; Scuseria, G. E.; Robb, M. A.; Cheeseman, J. R.; Scalmani, G.; Barone, V.; Mennucci, B.; Petersson, G. A.; Nakatsuji, H.; Caricato, M.; Li, X.; Hratchian, H. P.; Izmaylov, A. F.; Bloino, J.; Zheng, G.; Sonnenberg, J. L.; Hada, M.; Ehara, M.; Toyota, K.; Fukuda, R.; Hasegawa, J.; Ishida, M.; Nakajima, T.; Honda, Y.; Kitao, O.; Nakai, H.; Vreven, T.; Montgomery, J. A.; Peralta, J. J. E.; Ogliaro, F.; Bearpark, M.; Heyd, J. J.; Brothers, E.; Kudin, K. N.; Staroverov, V. N.; Kobayashi, R.; Normand, J.; Raghavachari, K.; Rendell, A.; Burant, J. C.; Iyengar, S. S.; Tomasi, J.; Cossi, M.; Rega, N.; Millam, J. M.; Klene, M.; Knox, J. E.; Cross, J. B.; Bakken, V.; Adamo, C.; Jaramillo, J.; Gomperts, R.; Stratmann, R. E.; Yazyev, O.; Austin, A. J.; Cammi, R.; Pomelli, C.; Ochterski, J. W.; Martin, R. L.; Morokuma, K.; Zakrzewski, V. G.; Voth, G. A.; Salvador, P.; Dannenberg, J. J.; Dapprich, S.; Daniels, A. D.; Farkas, Ö.; Foresman, J. B.; Ortiz, J. V.; Cioslowski, J.; Fox, D. J. *Gaussian 09*, 01; Wallingford CT, 2009.
7. Adamo, C.; Barone, V., Toward Reliable Density Functional Methods without Adjustable Parameters: The PBE0 Model. *J. Chem. Phys.* **1999,** *110* (13), 6158-6170.
8. Hay, P. J.; Wadt, W. R., Ab Initio Effective Core Potentials for Molecular Calculations. Potentials for the Transition Metal Atoms Sc to Hg. *J. Chem. Phys.* **1985,** *82* (1), 270-283.
9. Schäfer, A.; Huber, C.; Ahlrichs, R., Fully Optimized Contracted Gaussian Basis Sets of Triple Zeta Valence Quality for Atoms Li to Kr. *J. Chem. Phys.* **1994,** *100* (8), 5829-5835.
10. te Velde, G.; Bickelhaupt, F. M.; Baerends, E. J.; Fonseca Guerra, C.; van Gisbergen, S. J. A.; Snijders, J. G.; Ziegler, T., Chemistry with ADF. *J. Comput. Chem.* **2001,** *22* (9), 931-967.
11. Lenthe, E. v.; Baerends, E. J.; Snijders, J. G., Relativistic regular two-component Hamiltonians. *J. Chem. Phys.* **1993,** *99* (6), 4597-4610.
12. van Lenthe, E.; Baerends, E. J.; Snijders, J. G., Relativistic Total Energy using Regular Approximations. *J. Chem. Phys.* **1994,** *101* (11), 9783-9792.
13. van Lenthe, E.; Ehlers, A.; Baerends, E.-J., Geometry Optimizations in the Zero Order Regular Approximation for Relativistic Effects. *J. Chem. Phys.* **1999,** *110* (18), 8943-8953.
14. van Lenthe, E.; Snijders, J. G.; Baerends, E. J., The Zero-Order Regular Approximation for Relativistic Effects: The Effect of Spin–Orbit Coupling in Closed Shell Molecules. *J. Chem. Phys.* **1996,** *105* (15), 6505-6516.
15. van Lenthe, E.; van Leeuwen, R.; Baerends, E. J.; Snijders, J. G., Relativistic Regular Two-Component Hamiltonians. *Int. J. Quantum Chem.* **1998,** *57* (3), 281-293.
16. Shaka, A. J.; Keeler, J.; Freeman, R., Evaluation of a New Broadband Decoupling Sequence: WALTZ-16. *J. Magn. Reson.* **1983,** *53* (2), 313-340.
17. Shaka, A. J.; Keeler, J.; Frenkiel, T.; Freeman, R., An Improved Sequence for Broadband Decoupling: WALTZ-16. *J. Magn. Reson.* **1983,** *52* (2), 335-338.

18. Pines, A.; Gibby, M. G.; Waugh, J. S., Proton-Enhanced NMR of Dilute Spins in Solids. *J. Chem. Phys.* **1973,** *59* (2), 569-590.
19. Peersen, O. B.; Wu, X. L.; Kustanovich, I.; Smith, S. O., Variable-Amplitude Cross-Polarization MAS NMR. *J. Magn. Reson. A* **1993,** *104* (3), 334-339.
20. Fung, B. M.; Khitrin, A. K.; Ermolaev, K., An Improved Broadband Decoupling Sequence for Liquid Crystals and Solids. *J. Magn. Reson.* **2000,** *142* (1), 97-101.
21. Duer, M. J., *Introduction to Solid-State NMR Spectroscopy*. Blackwell Publishing: Vicotria, Australia, 2004.
22. Widdifield, C. M.; Schurko, R. W., Understanding Chemical Shielding Tensors Using Group Theory, MO Analysis, and Modern Density-Functional Theory. *Conc. Magn. Reson. A* **2009,** *34A* (2), 91-123.
23. Lantto, P.; Vaara, J.; Kantola, A. M.; Telkki, V.-V.; Schimmelpfennig, B.; Ruud, K.; Jokisaari, J., Relativistic Spin−Orbit Coupling Effects on Secondary Isotope Shifts of ^{13}C Nuclear Shielding in CX_2 (X = O, S, Se, Te). *J. Am. Chem. Soc.* **2002,** *124* (11), 2762-2771.
24. Vícha, J.; Komorovsky, S.; Repisky, M.; Marek, R.; Straka, M., Relativistic Spin–Orbit Heavy Atom on the Light Atom NMR Chemical Shifts: General Trends Across the Periodic Table Explained. *J. Chem. Theory Comput.* **2018,** *14* (6), 3025-3039.
25. Rossini, A. J.; Schlagnitweit, J.; Lesage, A.; Emsley, L., High-resolution NMR of hydrogen in organic solids by DNP enhanced natural abundance deuterium spectroscopy. *J. Magn. Reson.* **2015,** *259*, 192-198.
26. Daube, D.; Aladin, V.; Heiliger, J.; Wittmann, J. J.; Barthelmes, D.; Bengs, C.; Schwalbe, H.; Corzilius, B., Heteronuclear Cross-Relaxation under Solid-State Dynamic Nuclear Polarization. *J. Am. Chem. Soc.* **2016,** *138* (51), 16572-16575.
27. Zagdoun, A.; Rossini, A. J.; Conley, M. P.; Grüning, W. R.; Schwarzwälder, M.; Lelli, M.; Franks, W. T.; Oschkinat, H.; Copéret, C.; Emsley, L.; Lesage, A., Improved Dynamic Nuclear Polarization Surface-Enhanced NMR Spectroscopy through Controlled Incorporation of Deuterated Functional Groups. *Angew. Chem. Int. Ed.* **2013,** *52* (4), 1222-1225.